PCCP

Accepted Manuscript

This article can be cited before page numbers have been issued, to do this please use: S. K. Balakrishnamurthy, S. K. Kalpathy and S. Anandhan, *Phys. Chem. Chem. Phys.*, 2018, DOI: 10.1039/C7CP07435B.

View Article Online
DOI: 10.1039/C7CP07435B

Synergism of *fictitious* forces on nickel cobaltite nanofibers: Electrospinning forces revisited

B. Sachin Kumar[1], Sreeram K. Kalpathy[2], S. Anandhan[1*]

[1]Department of Metallurgical and Materials Engineering, National Institute of Technology Karnataka, Mangaluru 575025, India.

[2]Department of Metallurgical and Materials Engineering, Indian Institute of Technology Madras, Chennai 600036, India.

[*]Corresponding author, email id: anandtmg@gmail.com
Phone number: +91-824-2473762

View Article Online
DOI: 10.1039/C7CP07435B

Abstract

Randomly oriented nanofibers of nickel cobaltite (NCO) were fabricated using sol-gel electrospinning followed by calcination. The precursor fibers were collected on rotating disc (RDI) and rotating drum (RDR) collectors. The variable *fictitious* forces produce continuous deflection at each fiber landing position on the RDI collector, which subjects the nanofibers to non-bundling. On the other hand, in case of RDR collector, the *fictitious* forces act just at the surface, and these forces merely cause slip of fibers along the rotational axis of RDR. This slip along with the retained *Columbic* charges on the surface of the fiber produces fiber bundling, which affects morphological and structural properties of the NCO nanofibers obtained by calcining the precursor fibers. Use of RDI collector in sol-gel electrospinning is a simple and optimal method of fabricating precursor nanofibers, which yields non-agglomerated, impurity-free inorganic nanofibers.

Keywords: *Coriolis*, electrospinning, collector, nickel cobaltite

List of Acronyms

Acronym	**Description**
1D	One dimensional
NCO	Nickel cobaltite
RDR	Rotating drum
RDI	Rotating disc
RDR_p	Precursor fibers collected over RDR collector
RDI_p	Precursor fibers collected over RDI collector
RDR_c	Calcined nanofibers obtained from calcination of RDR_p
RDI_c	Calcined nanofibers obtained from calcination of RDI_p
AFD	Average fiber diameter
SD	Standard deviation of fiber diameter
C_{FU}	Coefficient of fiber uniformity
BET	Brunauer-Emmett-Teller
SSA	Specific surface area
FWHM	Full-width at half maximum
DoA	Degree of Alignment
DoR	Degree of Randomness

View Article Online
DOI: 10.1039/C7CP07435B

1. Introduction

Sol-gel assisted electrospinning is a versatile and *tailor-made* 1D nanostructure synthesis technique, which gives a direct control over the stoichiometry, dimensionality and size of inorganic compounds for multifunctional applications.[1,2] The process involves three major steps: (i) preparation of stable *sol* using *sol-gel* chemistry with the help of suitable polymeric binder and salts, (ii) fabrication of precursor fibers by electrospinning, to obtain defect-free uniform nanofibers, and finally (iii) calcination of the precursor fibers to remove organic matter selectively, for obtaining inorganic nanofibers.

Apart from *sol-gel* chemistry or solution parameter[3] control, it is very important to have control over the electrospinning process parameters, as they play a vital role in size reduction of fibers, which in turn influence the functional properties of the desired material.[1] Many efforts have been made over decades to optimize these parameters.[4] Some of these process parameters are: voltage, flow rate of the *sol*, spinneret (single, multiple, needless), collector (material, geometry), spinneret tip to collector distance, temperature, humidity, and air/gas flow in electrospinning chamber.[5,6] However, in the present study, the focus is on the effect of type of collector used on the morphology of nanofibers.

Some applications demand a well-defined alignment of fibers, which is fulfilled by electrostatic, magnetic or mechanical means.[7,8] The commonly used mechanical approach is RDR collector, which reduces the diameter of fibers and aligns them along the direction of drum rotation.[3,9] This strategy may be undesirable for the synthesis of inorganic nanofibers such as NCO ($NiCo_2O_4$) as they agglomerate during the calcination. Besides, the increase in applied voltage or spinneret to collector distance and the presence of additives has been reported to vary the fiber diameter.[3,10,11] However, such cases lead to fibre bundling and alignment,[12] and thus the desired fiber morphology could not be attained. The objective of

View Article Online
DOI: 10.1039/C7CP07435B

this study is to eliminate such defects, and obtain uniform and ultrafine inorganic nanofibers by suitably tailoring the *fictitious* forces over the collector.

It is a well-known fact that *fictitious* forces such as centrifugal and *Coriolis* forces are always associated with any relative motion in which there is a rotating non-internal frame of reference. Various attempts have made in modelling and understanding the mechanism of these *fictitious* forces during centrifugal spinning or force-spinning of nanofibers to obtain aligned fiber mats.[13–16] These *fictitious* forces, which act at the jet initiation (rotating spinneret and static collector) play a vital role in forming deflected spiral paths, stretching the fibers and control thus morphology of the nanofibers. However, the fiber diameters obtained from centrifugal spinning are typically larger than those from electrospinning due to insufficient stretching in the absence of electric field.[17] In this study, using electrospinning and two different kinds of collector, i.e. RDR and RDI collector, an attempt has been made to study the synergism of *fictitious* forces on the morphology (dimensionality and directionality) of precursor nanofibers, and thereby the morphological and structural properties of NCO nanofibers, after calcination.

2. Experimental details

2.1. Preparation of sol

Stoichiometric proportions (with a total mass of 2 g) of anhydrous (dried under vacuum oven for 1 h) nickel acetate and cobalt acetate (Sisco Research Laboratories Private Limited, India) were dissolved in 10 mL of N, N-dimethyl formamide (Sisco Research Laboratories Private Limited, India). 2g of poly(styrene-*co*-acrylonitrile), having viscosity average molar mass of 2,460 kg·mol^{-1} (Bhansali Engineering Polymers, India) was added to the above solution such that the total salt to polymer wt ratio is unity. This solution was stirred in a closed vial for ~12 h to attain homogeneity.

View Article Online
DOI: 10.1039/C7CP07435B

2.2. Fabrication of precursor nanofibers

A single spinneret vertical electrospinning unit (e-spin nano, Physics Equipments Co., India) was used to fabricate the precursor nanofibers using two types of collectors (Figure 1a and b). The rotating disc collector was indigenously built, whose fiber collector dimension was ⌀10 cm × 1 cm with the same weight as RDI, whereas the rotating drum collector (⌀5 cm × 13 cm) was procured from Physics Equipment Co., India. The precursor fibers obtained from a static collector were spun on stationary RDI collector. The optimal electrospinning parameters were fixed as: spinneret tip to collector distance = 17 cm, flow rate = 1 $mL \cdot h^{-1}$, applied voltage = 25 kV, and the rotating speed of both the RDR and RDI was kept at 500 rpm. The electrospun fibers were collected for a fixed duration on all the collectors. The precursor fibers were collected on aluminium foil tagged to all types of collector. Later, these precursor fibers were carefully peeled off the foil and calcined.

2.3. Calcination of precursor nanofibers

The electrospun nanofiber mat was placed on a quartz plate in a programmable Muffle furnace (Indfurr, India) at 500°C. The calcination soaking time was 2 h and a heating rate of $2°C \cdot min^{-1}$ was used for calcination. The resulting oxide fibers were left in the furnace to anneal till room temperature and then collected for characterization.

2.4. Characterization of nanofibers

The micrographs of the precursor and calcined nanofibers were obtained using a scanning electron microscope (SEM, JSM-6380LA, JEOL, Japan). The fibers were gold sputtered with a sputter machine (JFC 1600 autofine coater, JEOL. Japan) prior to imaging. The fiber diameter and alignment (directionality tool) were measured (Fiji ImageJ, 1.51n, National Institutes of Health, USA) defined in terms of DoR and DoA as[18]:

$$DoA = 1 - DoR = 1 - \left(\frac{dispersion}{90} \right) \quad (1)$$

The fiber diameter was measured at three different spots of 50 fibers at random locations on the fiber mat, and an average of those 150 values is reported for each sample. Apart from SD, the fiber uniformity was estimated as a factor of C_{FU}.[19] Furthermore, the SSA of calcined nanofibers were measured by the BET method, after degassing the samples for 5 h at 150°C under high vacuum (Autosorb 1C, Quantachrome Instruments, USA). High-resolution micrographs of calcined nanofibers were recorded using field-emission scanning electron microscope (FESEM, ULTRA 55, Gemini, Carl Zeiss, Germany).

Structural characterization of calcined nanofibers was done using X-ray diffractometer (X'Pert PRO, PANalytical, Netherlands) and micro-Raman spectrometer (LabRAM HR, Horiba, Japan). X-ray diffraction (XRD) patterns were recorded using Cu K_α radiation (wavelength, λ = 0.154 nm) for 2θ = 10-80° (0.5° per minute), at an operating voltage and current of 30 kV and 20 mA, respectively. The raw XRD patterns were profile fitted using Pseudo Voigt I function, in OriginPro 2016 (Sr1, OriginLab Corporation, USA). The instrumental broadening was accounted for using bulk silicon sample and subtracted from the measured FWHM to obtain the actual FWHM. The crystallite shape was assumed to be spherical from FESEM and hence, the dimensionless shape factor (k) was set to 0.9 in *Scherrer* equation, and the *Williamson-Hall* plot was used to calculate crystallite sizes of samples. Raman spectra were obtained using diode-pumped solid-state laser source, at a power of 28 mW and wavelength of 532 nm. Lorentzian function was used to deconvolute Raman spectra using OriginPro 2016 software.

View Article Online
DOI: 10.1039/C7CP07435B

3. Results and discussion

3.1. SEM results

3.1.1 Precursor nanofibers

The diameter and alignment of the precursor nanofibers is affected by the electrostatic interaction of the surface cations on the fiber during whipping, and the mechanical drawing of the fiber by the collector. Accordingly, from Figure 2, the AFD and SD of the precursor nanofibers is observed to be the least for the RDI collector. Conversely, the larger AFD and SD of the fibers from the static collector is due to the role of the mechanical drawing process by the rotating collectors (Figure 2a and d). However, the alignment of nanofibers in the static collector is a result of fiber bundling during spinning due to the increase in conductivity of the sol. This causes an insufficient stretching of nanofibers during whipping, resulting in high value of SD and C_{FU} in the static collector, which indicates non-uniformity in fiber diameter. Hence, the precursor fibers obtained using static collector exhibit a high degree of fiber alignment. From Figure 2g and h, it is observed that DoA of RDR_p was less in comparison with that of the static collector. This could be due to the slip caused during the winding of fibers onto the surface of the RDR collector, which is also evident from SD and C_{FU} of fibers. Further, the DoA, AFD, SD, and C_{FU} of fibers spun on RDI were found to be the least (Figure 2f and i), which are the essential parameters to form non-agglomerated, ultrathin calcined fibers. The least DoA and high DoR in RDI_p were due presumably to the action of *fictitious* forces, which are considered in detail in section 3.3.

3.1.2 Calcined nanofibers

Figure 3a and b, show the electron micrographs of calcined nanofibers obtained from the RDR and RDI collectors, respectively. Calcined fibers obtained from RDR collected fibers were found to have large AFD and SD than their precursor fibers (Figure 2e) due to the acute

agglomeration of well-aligned adjacent nanofibers. This in turn shoots up the C_{FU} (Figure 3c), and thus decreases the fiber uniformity. However, in case of RDI collector, the DoR of fibers has increased up to 14% due to the thermally induced wrinkling of agglomerated fibers during the calcination as the precursor fibers shrink, liberating organic volatiles. From Figure 3d, the AFD and SD of the RDI_c nanofibers were found to be lesser than their RDI_p. This observation implies that the fibers did not agglomerate much, and retained their morphology even after calcination. However, increase in C_{FU} of RDI_c nanofibers suggests the unavoidable agglomeration and segregation (by diffusion) during the calcination process, which is significantly less compared to that of RDR_c nanofibers. Here, an increase in DoR of about 11% was calculated, which is due to the thermally induced fiber wrinkling; this might be due to the increased intersection of nanofibers deposited on RDI collector. The randomly oriented fibers tend to have large number of intersections with other fibers as compared to the aligned ones (Figure 2b and c), which could constrain the wrinkling of precursor nanofibers during the calcination process. Hence, the calcined nanofibers obtained using RDI collector have the least AFD and SD, and comparatively better fiber uniformity. This plays a significant role in the structural and functional properties of the inorganic nano-fibrous material.

The SSA of RDR_c and RDI_c nanofibers are tabulated in Table 1. The increase in surface area of RDI_c nanofibers is attributed to the reduction in their AFD as well as porous morphology due to the NCO nanoparticles embedded along the nanofibers. These values are comparable with the NCO based nanofibers/nanobelts reported hitherto in literature.[20,21] The improved SSA of RDI_c nanofibers is expected to improve their functional properties such as electrocatalytic performance.

View Article Online
DOI: 10.1039/C7CP07435B

3.1.3 FESEM results

High resolution FESEM images of the inorganic nanofibers (Figure 4) were examined to observe the nanoparticle morphology along the calcined nanofibers obtained using both RDR and RDI collectors. In case of RDR_c nanofibers, the nanoparticles are densely packed and agglomerated, leading to less macro porosity. However, the RDI_c nanofibers have a highly porous structure with well distinguished near-spherical nanoparticles, decorated similar to a *cephalopod limb* along the fiber. This could make RDI_c nanofibers a potential candidate for catalytic applications. Furthermore, the morphological changes observed in RDR_c and RDI_c nanofibers is a function of *fictitious* forces acting on their respective precursor fibers, which forms a subset of the electrospinning process parameters. This suggests that the use of RDI collector might be extended to metal oxide nanofibers of other transition metals as well.

3.2. Structural characterization of the inorganic nanofibers

3.2.1 XRD analysis

In Figure 5, XRD patterns obtained for both RDR_c and RDI_c nanofibers revealed the presence of crystalline NCO indexed to *the International Centre for diffraction Data* (ICDD) file no. 00-073-1702. In case of RDR_c nanofibers, the presence of crystalline $NiCoO_2$ was observed, which matches with the ICDD file no. 01-010-0188. Further, the presence of an additional peak ca. 51.5° with some coinciding peaks of NCO hints the formation of crystalline A_2O_3 in the RDR_c nanofibers. The cation A, represents both Ni (ICDD file no. 00-014-0481) and Co (ICDD file no. 00-002-0770) ions. The formation of $NiCoO_2$ and A_2O_3 may be attributed to two-stage *redox* reaction.

When the fibers agglomerate in RDR_p nanofibers during calcination, probably the sub-products are entrapped within fiber along with NCO particles to a greater extent. At this stage, *carbothermal/NO_x reduction* of NCO takes place in the presence of by-products of precursor to form $NiCoO_2$, Ni^0, and Co^0.[22–26] Subsequently, these Ni^0 and Co^0 in the presence

of excess oxygen due to the entrapment of oxygen bearing groups like acetate from precursor. give Ni_2O_3 and Co_2O_3. Hence, the overall *redox* reaction can be written as:

$$3NiCo_2O_4 \xrightarrow{\Delta/O_2/C/CO/NO_x} NiCoO_2 + Ni_2O_3 + Co_2O_3 + CO_y + NO_z \quad (1)$$

Scherrer equation and *Williamson-Hall* plot (Figure 6) were used to measure the crystallite size and microstrain (ε) in both RDR_c and RDI_c nanofibers and tabulated in Table 1. The *Scherrer* equation does not account for the thermally induced microstrain in the crystal lattice and hence, the *Williamson-Hall* plot is more appropriate for finding the crystallite size. It was observed that there is no significant change in the crystallite size of NCO in both RDR_c and RDI_c nanofibers. However, the lattice strain is marginally higher in RDI_c than RDR_c nanofibers. In comparison, the $NiCoO_2$ lattice has almost no strain. This suggests the formation of $NiCoO_2$ from NCO crystals. Also, it is a well-known fact that nanostructures have more lattice strains due to defects. Since RDI_c has an overwhelming population of well-defined NCO particles in comparison with the RDR_c nanofibers, the crystallites in the former could be under high lattice strain.

3.2.2 Raman analysis

To understand the presence of the non-crystalline phase of oxides in calcined nanofibers, Raman spectra were obtained for both RDR_c and RDI_c NCO nanofibers (Figure 7). Five Raman active modes (A_{1g}+E_{2g}+$3F_{2g}$) were observed for both the RDR_c and RDI_c nanofibers, confirming the crystalline phase of NCO.[27] A broad shoulder peak was observed ca. 650 cm^{-1} which suggests the formation of amorphous phase of NCO.[28] It has been reported that a broad peak ca. 530 cm^{-1} is a distinct characteristic feature of $NiCoO_2$ in the literature.[29] However, this peak coincides with F_{2g} peak of NCO and remains indistinguishable. Further, in case of RDR_c nanofibers, four broad peaks in the range of 250-400 cm^{-1} were observed. These peaks appear also in the Raman spectra of A_2O_3 structures such as Cr_2O_3, Fe_2O_3 as per

literature.[30,31] As no specific study on Raman spectra of Ni_2O_3 and Co_2O_3 is available, and also since Raman signature is a structural property of the material, we may ascribe the observed Raman peaks to Ni_2O_3 and Co_2O_3 formed in RDR_c nanofibers.

It has been observed in literature that nanocrystallites confine optical phonons within them, if the surrounding medium (amorphous phases) of nanoparticles does not support the vibrational wave numbers in the material. As the nanoparticle size reduces, the amorphous phase increases (as there is an increase in crystallite boundary) and the electron-phonon interaction decreases, leading to broadening and shifting of peaks. Hence, the vibrational spectrum of nanoparticles deviates from that of their bulk counterparts. Raman spectroscopic investigations of such nanoparticles (typically less than 10 nm) have revealed such shifts in the Raman peaks along with asymmetric broadening.[32] From Figure 7, it is evident that the peaks of NCO (A_{1g}+E_{2g}+3F_{2g}) have not only shifted, but, asymmetric broadening is also observed for all F_{2g} peaks. This suggests that RDI_c nanofibers are made of pure NCO nanoparticles of high porosity and smaller size compared with the RDR_c nanofibers.

3.3. Mechanism of fiber morphology evolution

From SEM micrographs (Figure 2c and e) it was observed that, a larger DoR in fiber orientation has been generated for RDI_p even though the speed of rotation of both the collectors was fixed at 500 rpm. All the synthesis parameters of synthesis were kept constant for both RDI_p and RDR_p nanofibers. The variation in randomness of fiber orientation, and AFD in both RDR and RDI collectors can be explained in the light of physical forces governing the motion of the jet.

3.3.1 Effect of time of flight of fiber

The velocity of a fiber (v) arriving at the collector can be calculated using the following equation[33]:

View Article Online
DOI: 10.1039/C7CP07435B

$$t_f = \left(\frac{4w}{100\pi\rho v} \right) \times \frac{1}{A^2} \quad (2)$$

where w is the weight, ρ is the density, and A is the AFD. The time t_f represents the time of flight of the fiber to reach the collector. Now considering the equivalent fibers landing at the two different collectors, the time of flight of a fiber landing on the RDI collector is more than that taken by a fiber depositing on the RDR collector as AFD is less for the former, which was calculated earlier from SEM micrographs (Figure 2b and c). This suggests that the increase in time of flight of a fiber increases the drawing process of the fiber due to *Columbic* forces during whipping before it reaches the collector. Hence, fibers are wound faster along the RDR collector without much drawing effect as they enter the collector parallel to the axis of whipping (Figure 1a and 8a). On the other hand, in RDI collector, the fibers are pulled in the direction of whipping, which provides more scope for fiber drawing; that, in turn, produces fibers with lower AFD.

3.3.2 Synergism of fictitious forces on the fiber

Using a rotating frame of reference for the coordinate system, the governing equations of the system may be described by the continuity equation[34,35]:

$$\nabla \cdot u = 0, \quad (3)$$

where u is the relative velocity of the fiber jet per unit mass at the collector position (say, *R*) and the relevant momentum balance equation may be written as:

$$\frac{\partial u}{\partial t_f} + (u \cdot \nabla) u = -\frac{\nabla P}{\rho} + \frac{\nabla T}{\rho} + E(q) + A(\phi) + g - \Omega \times (\Omega \times R) - 2\Omega \times u, \quad (4)$$

where P is the pressure, ρ is the density of the fiber material, T is the stress tensor, E is the applied electric field, which is a function of Columbic charge (q) in the nanofiber, A is

the ambient environment, which is a function relative humidity (ϕ), g is the gravity effect. Ω is the angular velocity of the collector and R is the position vector describing the fiber position on collector. For both the RDR and RDI collectors, the first five terms on the right-hand side of Equation 4 remain the same and thus, the last two terms additionally affect the acceleration of the fiber on the collector.

The centrifugal acceleration term, $-\Omega\times(\Omega\times R)$, arises due to the rotation of collector; and the *Coriolis* acceleration $(-2\Omega\times u)$ arises due to the non-inertial frame of reference as the fiber rotates on its own axis relative to the collector rotation. The angular velocity vector, Ω, is pointed along the axis of rotation of the collector using the right-hand rule (Figure 8a and b) and its magnitude is given by:

$$|\Omega| = \frac{d\theta}{dt_f} = \omega(t_f), \tag{5}$$

where θ is the angle made by the trajectory in the inertial frame of reference (local frame) of fiber element. This trajectory is a straight line along the tangential path of fiber rotation. The position of the fiber element in (X,Y) coordinates for a given time of flight, t_f, is given by:

$$R_i(t_f) = vt_f(\cos\theta, \sin\theta), \tag{6}$$

where v is the actual velocity of the fiber element. Now in collector frame of reference, the XY axes rotate with an angular velocity of ω, so the trajectory is a non-linear curved path and expressed as:

$$R(t_f) = vt_f(\cos(\theta-\omega t_f), \sin(\theta-\omega t_f)). \tag{7}$$

Equation 7 represents the deflection of fiber element from its actual position on the collector. This deflection is a function of time of flight, position and velocity of the fiber element.

View Article Online
DOI: 10.1039/C7CP07435B

Hence, with different combinations of R, θ, and t_f, a wide range if various deflected trajectories are created along the variable radius of RDI. This wide range of deflected trajectories gives more randomness in the nanofibers collected on the RDI collector.

Furthermore, from Equation 7, for a given position (R, θ) and velocity (v), the deflection experienced by the fiber is directly proportional to the time of flight (t_f). In other words, with increase in time of flight of the fiber, the deflection of the fiber path on the collector is increased. And this helps in further drawing of the fiber before it lands on the collector, which in turn leads to decrease in AFD. This facilitates the observation drawn from section 3.3.1.

Using Equations 5 and 7, the centrifugal acceleration on the nanofiber can be expressed as[36]:

$$-\Omega\times\left(\Omega\times R\right)=\omega^2 vt_f\left(\cos(\theta-\omega t_f),\sin(\theta-\omega t_f)\right)=\omega^2 R(t_f) \tag{8}$$

and the *Coriolis* acceleration is expressed as follows:

$$-2(\Omega\times u)=2\omega v[\sin(\theta-\omega t_f),-\cos(\theta-\omega t_f)]-2\omega^2 R(t_f)\,. \tag{9}$$

Comparing Equations 8 and 9, the *Coriolis* acceleration opposes the centrifugal acceleration, and the net effect has two components, namely, $-\omega^2 R(t_f)$ corresponding to the circular motion at $R(t_f)$ (inward component directed towards the centre of rotation) and a perpendicular component $2\omega v[\sin(\theta-\omega t_f),-\cos(\theta-\omega t_f)]$ that is a function of the actual velocity of the fiber (v). Hence, the fiber in the RDI collector experiences a circular motion with an additional velocity perpendicular to its actual velocity. This increased velocity, in turn decreases the AFD of the fiber.

View Article Online
DOI: 10.1039/C7CP07435B

In case of RDR collector (Figure 8b), the non-inertial frame of reference of the fiber rotates only in a fixed distance (R = radius of the drum) around the axis of rotation in the inertial frame XY. Hence, the *Coriolis* deflection of Equation 7, results in slip (*wind-on angle,* ϕ) of fibers during the winding of fiber on the rotating drum and the constant *Coriolis* accelerations (as R is fixed for RDR) are tangential to the motion of the fiber, which creates a spiral path around the drum collector.[37,38] The mathematical formulations and effect of this slip have been discussed elsewhere in the literature.[39,40] The net effect is that it bundles up the fibers on the rotating drum to a large extent, and increases with increase in speed of the rotation of the drum collector. Thus, the *fictitious forces* play a vital role in reducing the fiber orientation and fiber diameter of the nanofibers. In other words, these *fictitious forces* affect the morphology of the precursor nanofibers. This also helps reduce agglomeration of inorganic nanofibers during calcination to attain least AFD of defect-free, uniform, and porous inorganic nanofibers. Also, it helps eliminate the formation of impurities due to phenomena such as phase separation.

4. Summary and conclusions

RDI_c fibers were uniform and less oriented with an AFD of ~117 nm. The *fictitious* forces played a remarkable role in the formation of high degree of randomly (DoR=34%) oriented fibers in case of RDI collector, and the effect was revisited in detail. The proper choice of collector must be made depending on the desired morphology and properties of the inorganic nanofibers to be fabricated using sol-gel assisted electrospinning. Less agglomerated and impurity-free NCO nanofibers were obtained using RDI collector, which had near-spherical NCO nanoparticles decorated along the nanofiber similar to the *suckers* of *cephalopod limb*, with a high porosity. The physics discussed here may possibly be extrapolated to other metal oxide nanofibers of the first-row transition metals for tailoring their structural and functional properties.

View Article Online
DOI: 10.1039/C7CP07435B

Funding information

No funding from any funding body has been received for this study.

Acknowledgments

B. S. Kumar is grateful to National Institute of Technology Karnataka (NITK), India, for a research fellowship. The characterization partly made use of funds from the new faculty initiation grant (No: MET/15-16/836/NFIG/SRER) to S.K. Kalpathy from Indian Institute of Technology Madras, India. The authors would like to thank Gurudath B, Metallurgical and Materials Engineering, NITK, India, for providing access to KeyShot software.

References

1. Y. Dai, W. Liu, E. Formo, Y. Sun and Y. Xia, Ceramic nanofibers fabricated by electrospinning and their applications in catalysis, environmental science, and energy technology, *Polym. Adv. Technol.*, 2011, **22**, 326–338.

2. J. Xue, J. Xie, W. Liu and Y. Xia, Electrospun Nanofibers: New Concepts, Materials, and Applications, *Acc. Chem. Res.*, 2017, **50**, 1976–1987.

3. B. Sachin Kumar, A. N. Prakrthi, T. Senthil, K. Udaya Bhat and S. Anandhan, Organoclay enabled nanofiber formation from a polyolefin elastomer, *Adv. Polym. Technol.*, 2016, 1-18.

4. W. Cui, X. Li, S. Zhou and J. Weng, Investigation on process parameters of electrospinning system through orthogonal experimental design, *J. Appl. Polym. Sci.*, 2007, **103**, 3105–3112.

5. S. Fakirov, *Nano-size Polymers: Preparation, Properties, Applications*, Springer, 2016.

6. S. Ramakrishna, K. Fujihara, W.-E. Teo, T.-C. Lim and Z. Ma, *An Introduction to Electrospinning and Nanofibers*, World Scientific, 2005.

7. W. E. Teo and S. Ramakrishna, A review on electrospinning design and nanofibre assemblies, *Nanotechnology*, 2006, **17**, R89.

8. D. Yang, B. Lu, Y. Zhao and X. Jiang, Fabrication of Aligned Fibrous Arrays by Magnetic Electrospinning, *Adv. Mater.*, 2007, **19**, 3702–3706.

9. P. Katta, M. Alessandro, R. D. Ramsier and G. Chase, Continuous Electro-Spinning of Aligned Polymer Nanofibers on a Wire Drum Collector, *Nano Lett.*, 2004, **4**, 2215–2218.

10. B. S. Kumar, A. M. Shanmugharaj, S. K. Kalpathy and S. Anandhan, Some new observations on the structural and phase evolution of nickel titanate nanofibers, *Ceram. Int.*, 2017, **43**, 6845–6857.

11. G. K. Arumugam, S. Khan and P. A. Heiden, Comparison of the Effects of an Ionic Liquid and Other Salts on the Properties of Electrospun Fibers, 2–Poly(vinyl alcohol), *Macromol. Mater. Eng.*, 2009, **294**, 45–53.

12. Q. Zhang, L. Wang, Z. Wei, X. Wang, S. Long and J. Yang, Large-scale aligned fiber mats prepared by salt-induced pulse electrospinning, *J. Polym. Sci. Part B Polym. Phys.*, 2012, **50**, 1004–1012.

13. H. Xu, H. Chen, X. Li, C. Liu and B. Yang, A comparative study of jet formation in nozzle- and nozzle-less centrifugal spinning systems, *J. Polym. Sci. Part B Polym. Phys.*, 2014, **52**, 1547–1559.

14. S. Padron, A. Fuentes, D. Caruntu and K. Lozano, Experimental study of nanofiber production through forcespinning, *J. Appl. Phys.*, 2013, **113**, 024318.

15. X. Zhang and Y. Lu, Centrifugal Spinning: An Alternative Approach to Fabricate Nanofibers at High Speed and Low Cost, *Polym. Rev.*, 2014, **54**, 677–701.

16. A. Valipouri, S. A. H. Ravandi, A. Pishevar and E. I. Părău, Experimental and numerical study on isolated and non-isolated jet behavior through centrifuge spinning system, *Int. J. Multiph. Flow*, 2015, **69**, 93–101.

17. C. Liu, J. Sun, M. Shao and B. Yang, A comparison of centrifugally-spun and electrospun regenerated silk fibroin nanofiber structures and properties, *RSC Adv.*, 2015, **5**, 98553–98558.

18. G. Cadafalch Gazquez, V. Smulders, S. A. Veldhuis, P. Wieringa, L. Moroni, B. A. Boukamp and J. E. ten Elshof, Influence of Solution Properties and Process Parameters on the Formation and Morphology of YSZ and NiO Ceramic Nanofibers by Electrospinning, *Nanomaterials*, 2017, **7**, 16.

19. G. George and S. Anandhan, Glass fiber–supported NiO nanofiber webs for reduction of CO and hydrocarbon emissions from diesel engine exhaust, *J. Mater. Res.*, 2014, **29**, 2451–2465.

20. L. Huang, W. Zhang, J. Xiang and Y. Huang, Porous $NiCo_2O_4$/C nanofibers replicated by cotton template as high-rate electrode materials for supercapacitors, *J. Materiomics*, 2016, **2**, 248–255.

21. L. Li, S. Peng, Y. Cheah, P. Teh, J. Wang, G. Wee, Y. Ko, C. Wong and M. Srinivasan, Electrospun Porous $NiCo_2O_4$ Nanotubes as Advanced Electrodes for Electrochemical Capacitors, *Chem. – Eur. J.*, 2013, **19**, 5892–5898.

22. S. Zhang, X. Zhu, C. Zheng, D. Hu, J. Zhang and X. Gao, Study on catalytic soot oxidation over spinel type ACo_2O_4 (A = Co, Ni, Cu, Zn) catalysts, *Aerosol Air Qual. Res.*, 2017, **17**, 2317-2327.

23. X. Wang, W. Wen, J. Mi, X. Li and R. Wang, The ordered mesoporous transition metal oxides for selective catalytic reduction of NO_x at low temperature, *Appl. Catal. B Environ.*, 2015, **176**, 454–463.

24. C. Alegre, C. Busacca, O. Di Blasi, V. Antonucci, A. S. Aricò, A. Di Blasi and V. Baglio, A combination of CoO and Co nanoparticles supported on electrospun carbon nanofibers as highly stable air electrodes, *J. Power Sources*, 2017, **364**, 101–109.

25. T. A. Nissinen, Y. Kiros, M. Gasik and M. Leskelä, $MnCo_2O_4$ Preparation by Microwave-Assisted Route Synthesis (MARS) and the Effect of Carbon Admixture, *Chem. Mater.*, 2003, **15**, 4974–4979.

26. M. V. Reddy, G. Prithvi, K. P. Loh and B. V. R. Chowdari, Li Storage and Impedance Spectroscopy Studies on Co_3O_4, CoO, and CoN for Li-Ion Batteries, *ACS Appl. Mater. Interfaces*, 2014, **6**, 680–690.

27. V. Venkatachalam, A. Alsalme, A. Alghamdi and R. Jayavel, Hexagonal-like $NiCo_2O_4$ nanostructure based high-performance supercapacitor electrodes, *Ionics*, 2017, **23**, 977–984.

28. G. Gouadec and P. Colomban, Raman Spectroscopy of nanomaterials: How spectra relate to disorder, particle size and mechanical properties, *Prog. Cryst. Growth Charact. Mater.*, 2007, **53**, 1–56.

29. X. Leng, Y. Shao, L. Wu, S. Wei, Z. Jiang, G. Wang, Q. Jiang and J. Lian, A unique porous architecture built by ultrathin wrinkled $NiCoO_2$/rGO/$NiCoO_2$ sandwich nanosheets for pseudocapacitance and Li ion storage, *J. Mater. Chem. A*, 2016, **4**, 10304–10313.

30. I. R. Beattie and T. R. Gilson, The single-crystal Raman spectra of nearly opaque materials. Iron(III) oxide and chromium(III) oxide, *J. Chem. Soc. Inorg. Phys. Theor.*, 1970, **0**, 980–986.

31. S.-H. Shim, T. S. Duffy, R. Jeanloz, C.-S. Yoo and V. Iota, Raman spectroscopy and x-ray diffraction of phase transitions in Cr_2O_3 to 61 GPa, *Phys. Rev. B*, 2004, **69**, 144107.

32. A. K. Arora, M. Rajalakshmi, R. Thoguluva and V. Sivasubramanian, Raman Spectroscopy of Optical Phonon Confinement in Nanostructured Materials, *J. Raman Spectrosc.*, 2007, **38**, 604–617.

33. H. Wang, H. Shao and X. Hu, Structure of silk fibroin fibers made by an electrospinning process from a silk fibroin aqueous solution, *J. Appl. Polym. Sci.*, 2006, **101**, 961–968.

34. Y.-Q. Wan, Q. Guo and N. Pan, Thermo-electro-hydrodynamic model for electrospinning process, *Int. J. Nonlinear Sci. Numer. Simul.*, 2011, **5**, 5–8.

35. S. Padron, D. I. Caruntu and K. Lozano, On 2D Forcespinning™ Modeling, 2011, 821–830.

36. Coriolis effect - New World Encyclopedia, http://www.newworldencyclopedia.org/entry/Coriolis_effect#cite_note-caution-5, (accessed October 7, 2017).

37. D. A. Wolf and R. P. Schwarz, *Analysis of gravity-induced particle motion and fluid perfusion flow in the NASA-designed rotating zero-head-space tissue culture vessel*, 1991.

38. A. E. D. Barr, 2—the Physics of Yarn Tensions and Balloon Shapes in Spinning, Winding and Similar Processes, *J. Text. Inst. Trans.*, 1960, **51**, T17–T38.

39. W. B. Fraser, T. K. Ghosh and S. K. Batra, On Unwinding Yarn from a Cylindrical Package, *Proc. R. Soc. Lond. Math. Phys. Eng. Sci.*, 1992, **436**, 479–498.

40. Xiang Ming Kong, C. D. Rahn and B. C. Goswami, Steady-State Unwinding of Yarn from Cylindrical Packages, *Text. Res. J.*, 1999, **69**, 292–306.

View Article Online
DOI: 10.1039/C7CP07435B

List of Tables

Captions to Figures

View Article Online
DOI: 10.1039/C7CP07435B

Table 1

Type of collector	SSA ($m^2 \cdot g^{-1}$)	**Phase**	***Scherrer* equation**	***Williamson-Hall* plot**	
			Crystallite size (nm)	*Crystallite size (nm)*	*Microstrain, ε (%)*
RDR	10.1	NCO	13.44	18.29	0.184
		$NiCoO_2$	15.12	15.89	0.024
RDI	24.0	NCO	12.65	18.34	0.222

View Article Online
DOI: 10.1039/C7CP07435B

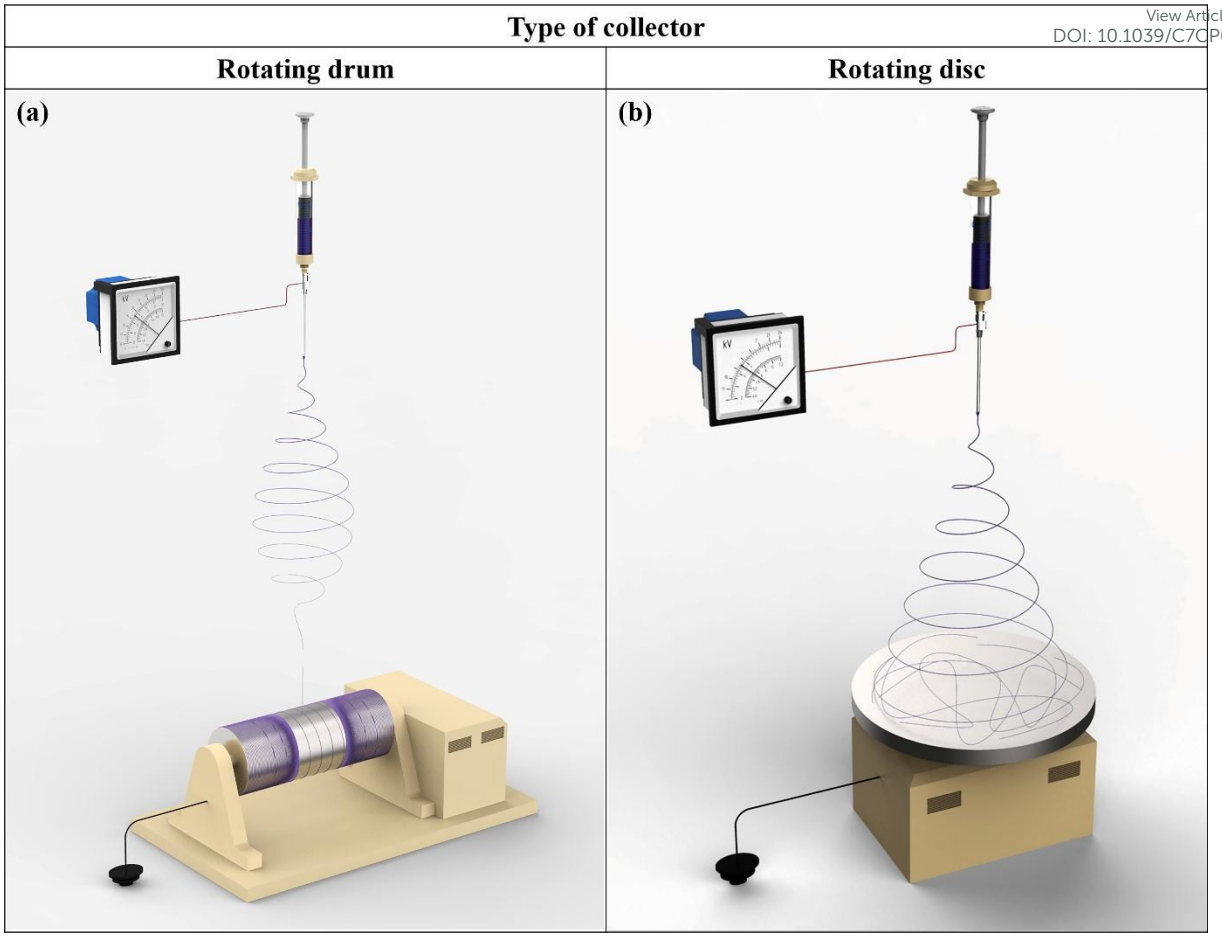

Figure 1

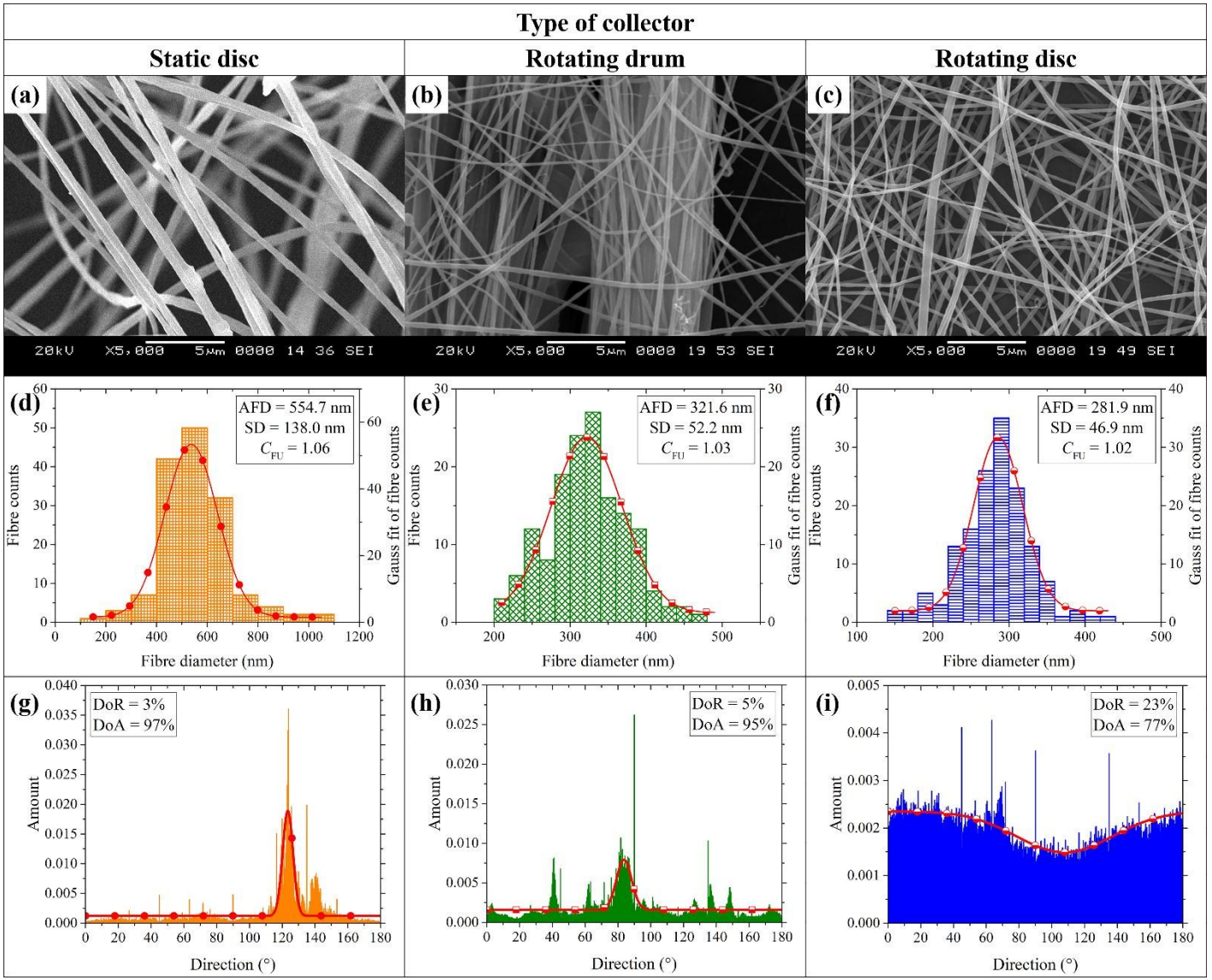

Figure 2

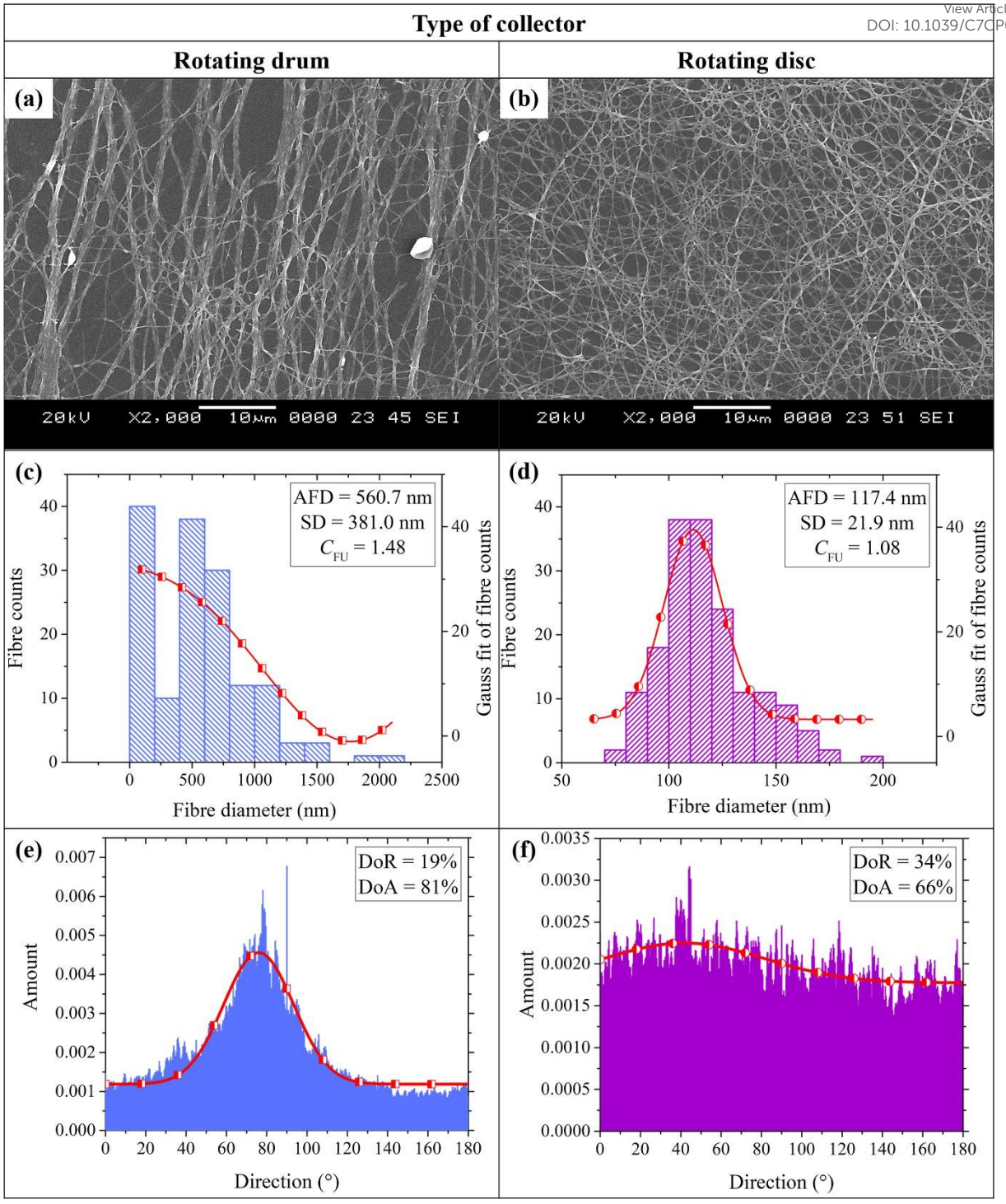

Figure 3

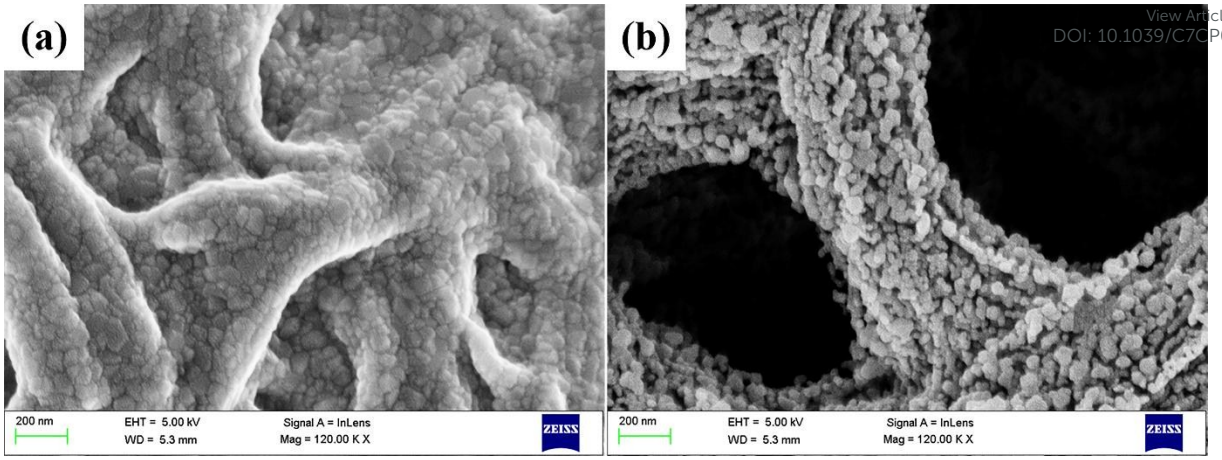

Figure 4

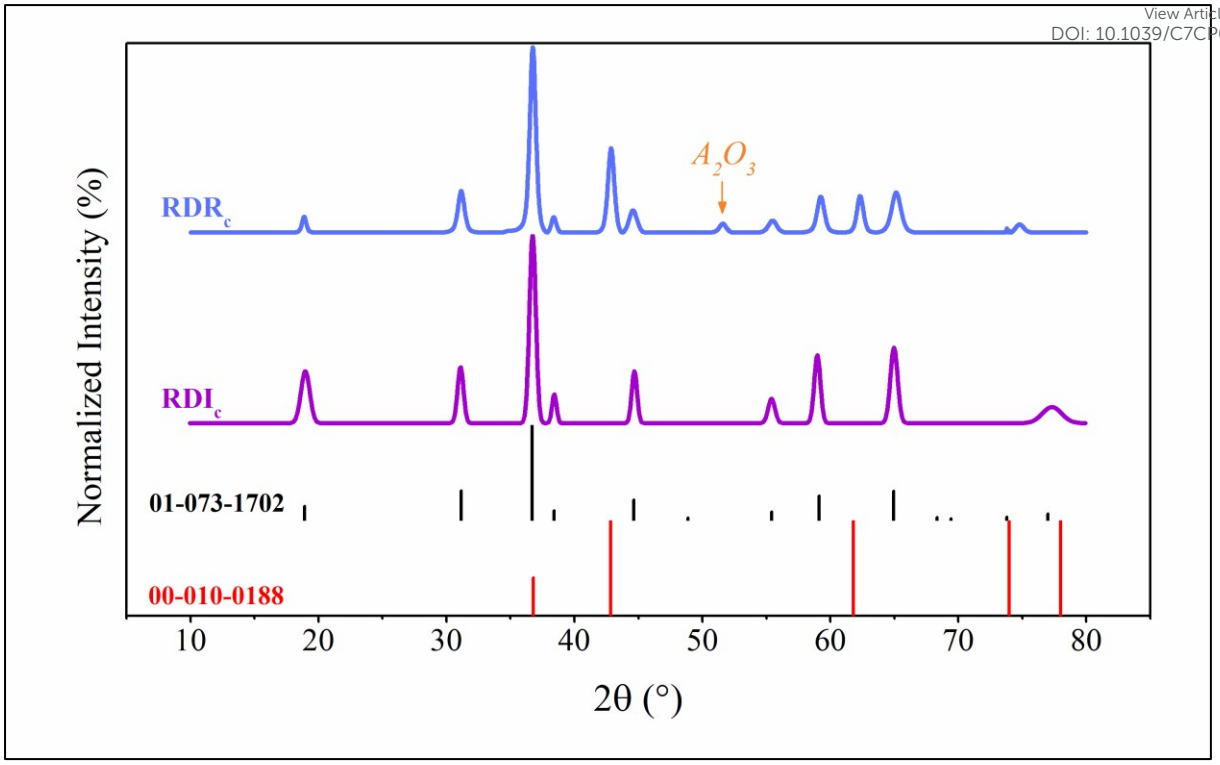

Figure 5

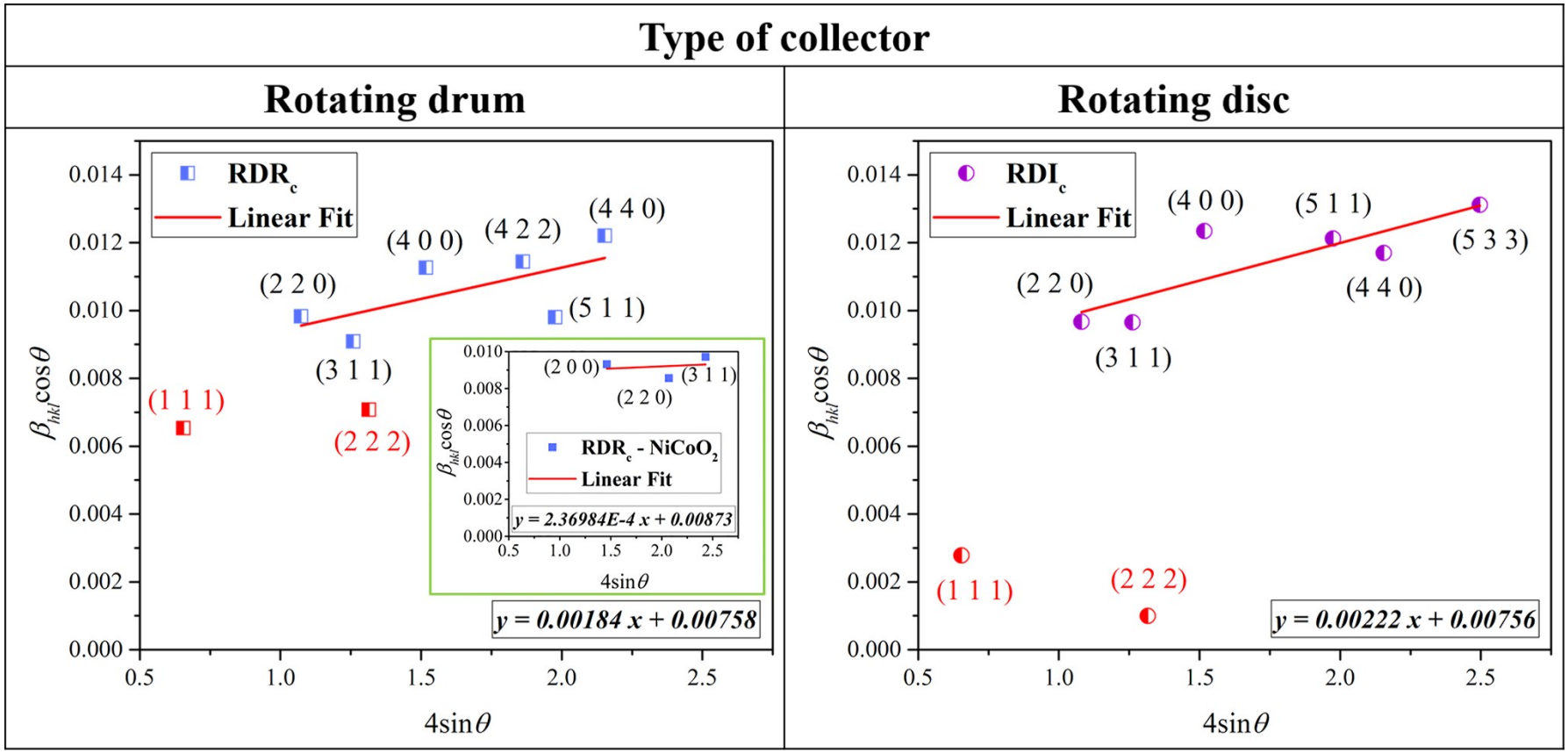

Figure 6

View Article Online
DOI: 10.1039/C7CP07435B

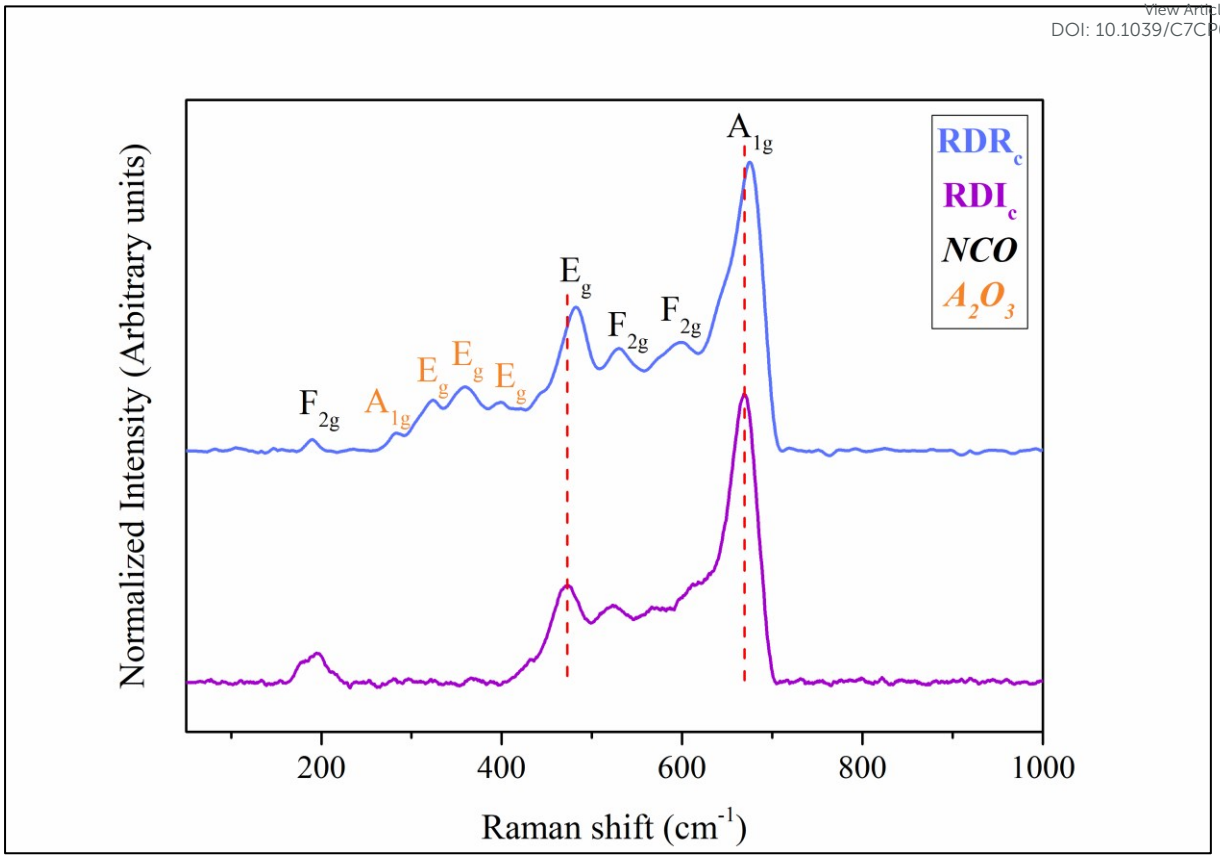

Figure 7

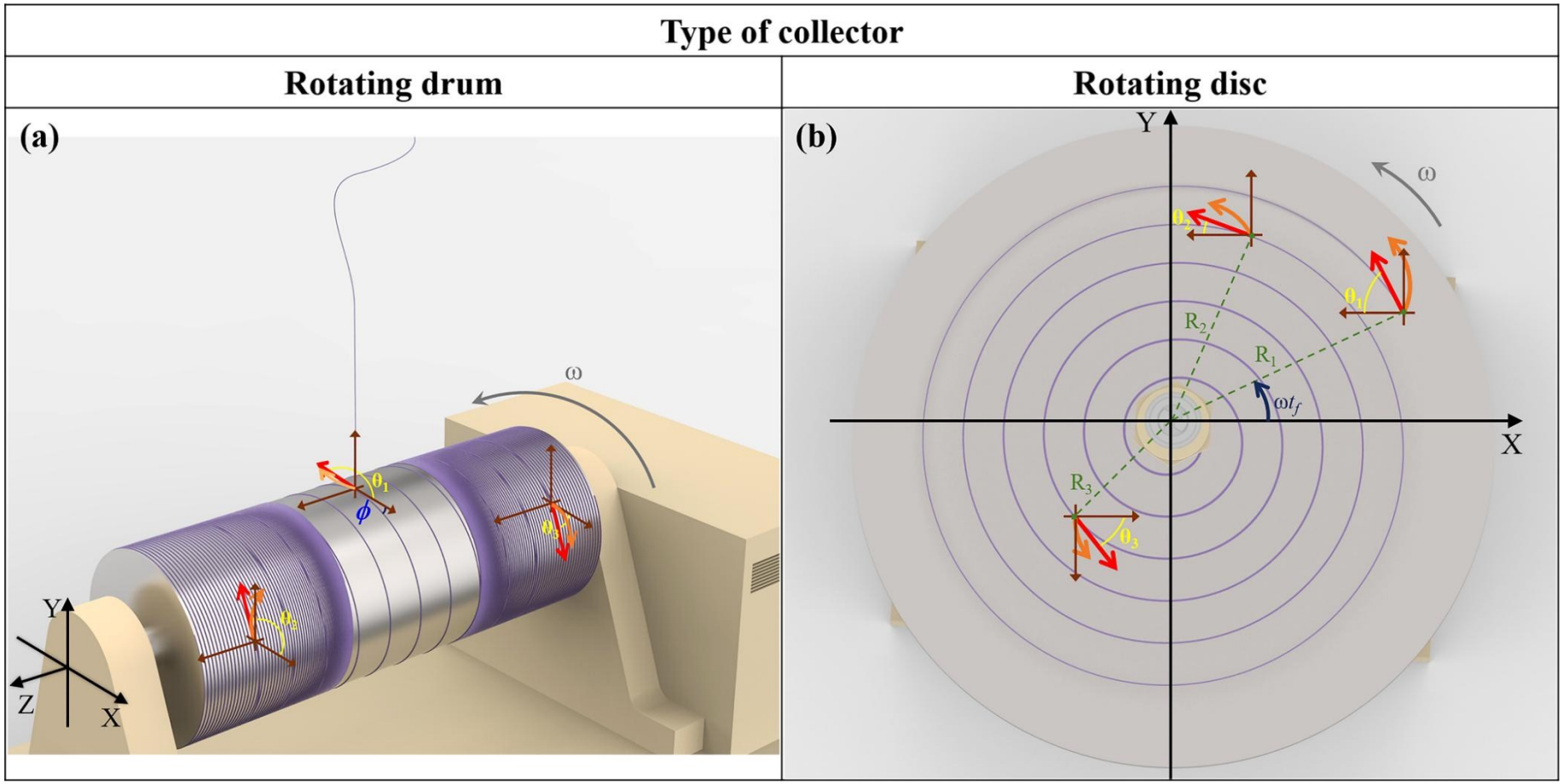

Figure 8

View Article Online
DOI: 10.1039/C7CP07435B

Graphical Abstract

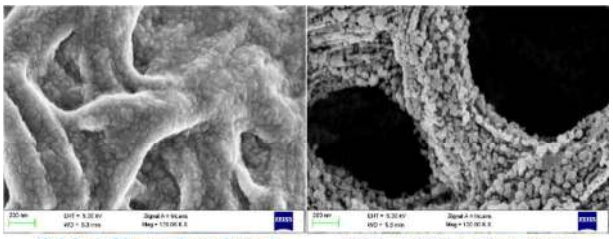

Highlight

Morphology and structure of electrospun $NiCo_2O_4$ nanofibers were tuned by an appropriate choice of collector and modifying relevant physical forces.